Reinvestigation of probertite, CaNa[B$_5$O$_7$(OH)$_4$]·3H$_2$O, a mineral commodity of boron

G. Diego Gatta[1], Enrico Cannaò[1], Valentina Gagliardi[2],

and Oscar Fabelo[3]

[1]Dipartimento di Scienze della Terra, Università degli Studi di Milano,
Via Botticelli 23, I-20133 Milano, Italy
[2]Istituto Gemmologico Italiano – IGI, Piazza S. Sepolcro 1, I-20123 Milano, Italy
[3]Institut Laue-Langevin, 71 Avenue des Martyrs, F-38000 Grenoble, France

Abstract

The crystal chemistry of probertite, a mineral commodity of B (B$_2$O$_3$ ~ 50 wt%) with ideal formula CaNa[B$_5$O$_7$(OH)$_4$]·3H$_2$O from the Kramer Deposit (Kern County, California – type locality), was investigated by a multi-methodological approach [*i.e.*, single-crystal X-ray (at 293 K) and neutron (at 20 K) diffraction, EPMA-WDS, LA-ICP-MS and LA-MC-ICP-MS]. As recently observed for other hydrous borates, the real chemical formula of probertite from the Kramer Deposit is virtually identical to the ideal one: the fraction of other elements is substantially insignificant. Therefore, excluding B, probertite does not act as geochemical trap of other industrially-relevant elements (*e.g.*, Li, Be or REE). The experimental findings of this study confirm that the structure of probertite is built up by the so-called pentaborate polyanion [B$_5$O$_7$(OH)$_4$]$^{3-}$(topology: 5(2Δ + 3T)], which consists of oxygen-sharing B-tetrahedra and -triangular units. The five (geometrical) components of the polyanion are: BO$_3$, BO$_2$OH, BO$_4$, BO$_3$OH and BO$_2$(OH)$_2$ groups. The pentaborate building units are connected to form infinite chains running along [100]. Clusters of distorted Ca-polyhedra [CaO$_5$(OH)$_3$(OH$_2$), CN = 9] and Na-polyhedra [NaO(OH)$_2$(OH$_2$)$_3$, CN = 6] are mutually connected by edge-sharing and, in turn, connected to the pentaborate chains by edge-sharing (with the Ca-polyhedron) and corner-sharing (with the Na-polyhedron). The H-bonding scheme in the structure of probertite is complex and pervasive, with 10 independent H sites (belonging to hydroxyl groups or H$_2$O molecule) and 11 over 14 oxygen sites involved in H-bonds as *donor* or *acceptors,* so that the H-bonding network presumably has an important role on the structural stability. The potential utilizations of probertite are discussed.

Keywords: Probertite, borates, mineral commodity, X-ray diffraction, neutron diffraction, crystal chemistry, hydrogen bonding.

2

Introduction

Probertite is one of the hydrous borates, with ideal chemical formula $CaNa[B_5O_7(OH)_4] \cdot 3H_2O$, usually found in sedimentary borate deposits along with the more common borax (ideal composition – i.c., $Na_2[B_4O_5(OH)_4] \cdot 8H_2O$), colemanite (i.c., $Ca[B_3O_4(OH)_3] \cdot H_2O$), ulexite (i.c., $NaCa[B_5O_6(OH)_6] \cdot 5H_2O$), kernite and tincalconite (i.c., $Na_6[B_4O_5(OH)_4]_3 \cdot 8H_2O$). Borates from this kind of deposits represent more than 90% of the borate minerals utilised by industry worldwide (U.S.G.S. 2019 and references therein). On the basis of its high economic importance and supply risk, boron is considered one of the "critical elements" (or "critical raw materials", according to the European Commission 2017). The worldwide production of borates is triplicated in the last 20 years (ca. 3 Mt in 1998, ca. 10 Mt in 2019), and the forecast predict the market to grow, in response to the raising request of B for several technologically relevant products (*e.g.*, heat-resistant glasses and ceramics, B-treated low-alloy steels, radiation-shielding materials, pharmaceutical and agricultural compounds). Among those, the radiation-shielding materials represent a market segment referred to nuclear reactors for energy production or scientific research, along with neutron sources for medical applications (*i.e.*, B neutron-capture therapy). B-bearing materials can offer an efficient radiation-shielding capacity, as ^{10}B shows a high capacity to absorb thermal neutrons due to its high cross section for the $^{10}B(n,\alpha)^7Li$ reaction (~3840 barns; Carter et al. 1953, Sears 1986, Palmer and Swihart 1996, Rauch and Waschkowski 2002). On the other hand, the neutron absorption capacity of ^{11}B is modest (cross section ~0.006 barns). In nature, about 20% of boron occurs as ^{10}B.

In the last years, we have investigated the crystal chemistry and the physical and chemical stability (at high/low temperature and high pressure, or leaching) of colemanite (Lotti et al. 2017, 2018, 2019), kurnakovite (ideally $Mg[B_3O_3(OH)_5] \cdot 5H_2O$, Gatta et al. 2019; Pagliaro et al. 2021), kernite (Comboni et al. 2020a; Gatta et al. 2020) and meyerhofferite (ideally $Ca_2[B_6O_6(OH)_{10}] \cdot 2H_2O$, Comboni et al. 2020b), using a multi-methodological approach. The aim of this paper is to extend our crystal-chemical investigation on borates to probertite, as one of naturally-occurring borates with the highest B-content (~50 wt% B_2O_3), by a multi-methodological approach based on single-crystal X-ray (at room conditions) and neutron diffraction (at low temperature: 20 K), electron microprobe analysis in wavelength-dispersive mode (EPMA-WDS) along with laser ablation - inductively mass spectrometry (LA-ICP-MS) and LA- multi collectors ICP-MS (LA-MC-ICP-MS), in order to provide: a) the chemical composition of probertite in terms of major, minor and trace components, along with the isotopic signature of B, b) the description of the B-coordination environment (*e.g.*, aplanarity of the triangular $BO_2(OH)$-group, polyhedral distortion of the tetrahedral $BO_2(OH)_2$-groups) and c) the location of all the proton sites, the description of their vibrational regime and the complex H-bonding scheme. As probertite

3

72   contains B, OH-groups and H_2O molecules (for a total of 25.7 wt% H_2O), it is an excellent candidate for

73   a neutron diffraction investigation. In addition, the H-bonding network in probertite structure is expected

74   to play an important (likely substantial) role on its thermal and compressional stability, which will be

75   investigated in the near future, affecting its potential use as B-aggregate in Portland or Sorel concretes.

76

Previous studies on probertite

78   Probertite is known since the beginning of the nineteenth century. The first studies on this mineral

79   were conducted by Eakle (1929), who provide the first chemical analysis of probertite, and by Barnes

80   (1949) and Clark and Christ (1959), who reported the unit-cell parameters and the potential space group

81   by single-crystal X-ray diffraction. Surprisingly, there is almost no data, based on modern standards,

82   about the chemical composition of probertite from the borates deposits worldwide in which it occurs.

83   The first (H-free) structural model of probertite was reported by Rumanova et al. (1966), on the basis of

84   X-ray intensity data collected by Weissemberg method, and later reinvestigated and improved by

85   Menchetti et al. (1982), using a single-crystal four-circle X-ray diffractometer, in the space group $P2_1/c$

86   with $a \cong 6.59$, $b \cong 12.56$, $c \cong 13.43$ Å, and $\beta \cong 99.97°$.

87   The fundamental building unit of the probertite structure is the pentaborate polyanion

88    $[B_5O_7(OH)_4]^{3-}$, shared with other borates (*e.g.*, ulexite), which consists of three tetrahedra and two

89   triangles [*i.e.*, 5(2Δ + 3T) topology], forming infinite chains running along [100] with a configuration

90   as that shown in Fig. 1. On this basis, probertite is classified as an ino-pentaborate (Strunz 1997).

91   The B-chains are connected by clusters of distorted Ca-polyhedra (with coordination number CN =

92   9) and Na-polyhedra (CN = 6), which are mutually connected by edge-sharing and, in turn, connected

93   to the pentaborate chains by edge-sharing (with the Ca-polyhedron) and corner-sharing (with the Na-

94   polyhedron) (Fig. 1). Menchetti et al. (1982) reported some differences in the individual triangular

95   B-O distances, without an explanation based on differences in the local environment of these bonds.

96   In addition, a first identification of the H_2O and OH-group was also given, with a potential location

97   of the H-sites. That of Menchetti et al. (1982) is the last investigation of the crystal structure of

98   probertite reported in the literature. More recently, Zhou et al. (2014) reported a density functional

99   theory study of the magnetic shielding mechanism for [11]B in probertite and Okutan et al. (2014)

100   described the electrical behaviour of probertite by dielectric spectroscopy.

101

102

103

104

4

Materials and Experimental methods

- *Probertite sample*

The sample of probertite investigated in this study belongs to the private collection of Dr. Renato Pagano (Italy), with ref. #11717. The hand specimen is made by a group of colorless to white, millimetric crystals, which are prismatic/acicular and elongated along [001]. The specimen comes from the Kramer Deposit, Mohave desert, Kern County, California, in which probertite coexists with other borates (*e.g.*, borax, colemanite, hydroboracite, inderite, inyoite, kernite, kurnakovite, meyerhofferite, searlesite, tincalconite, tunellite and ulexite; Noble 1926, Schaller 1930, Morgan and Erd, 1969, Puffer 1975). The Kramer Deposit is the type locality of the borate tunellite. A description of the Kramer deposit (with its extension, stratigraphy and mineralogy) is provided in Gatta et al. (2020).

- *Chemical characterization*

EPMA-WDS chemical micro-analyses were obtained with a JEOL 8200 Super Probe system at the Earth Sciences Department - University of Milan (ESD-MI), with operating conditions of 15 kV and 5nA, 5µm beam diameter, and counting times of 30s on the peaks and 10s on the backgrounds. Natural crystals were used as standards and the results were corrected for matrix effects using a *ZAF* routine, implemented in the JEOL suite of programs. The standards used were: grossular (Al, Si, Ca), forsterite-154 (Mg), fayalite-143 (Fe), K-feldspar (K), omphacite (Na), sanbornite (Ba), celestine (Sr), apatite (F). Only Ca, Na and Sr were observed at a significant level. The measured concentration of Ca and Na was virtually identical to the ideal one expected in probertite, *i.e.*, CaO 15.8(2) wt% and Na_2O 8.6(3) wt%, whereas that of (elemental) Sr ranging between 800 and 1000 wt ppm. A modest degeneration of the sample was observed under the electron beam.

Trace element concentration was determined at the Geochemistry, Geochronology and Isotope Geology laboratory of the ESD-MI by LA-ICP-MS. The instrument couples an Analyte Excite 193 nm ArF excimer laser microprobe system, equipped with an HelEx II volume sample chamber (Teledyne Cetac Technologies) to a single-collector quadrupole ICP-MS (iCAP RQ; Thermo Fischer Scientific). The NIST SRM 612 synthetic glass and ^{43}Ca were used as external and internal standards, respectively. Quality control of the analyses was achieved analyzing the USGS reference basalt glasses GSD-2G and BCR-2G (as references) together with the unknown. Precision was better than 5% and accuracy was within 2σ. A laser fluence of 2.5 J/cm^2 and a repetition rate of 5-10 Hz were set for both standard, references and probertite. The laser spot size was set to 85 µm, in order to minimize the limits of detection. The He flow rate was set to 0.5 L/min into the sample

5

138 chamber and to 0.2 L/min and in the HelEx II cup. Each analysis consisted in the acquisition of 40s

139 of background signal, about 60s of laser signal and 20s of wash out time. Data reduction was carried

140 out using the *Glitter* software package (Griffin et al. 2008).

141   The B isotopic composition of probertite has been measured *in-situ* using the same laser

142 system used for the determination of the trace element concentrations, connected with a double

143 focusing multi-collector (MC) ICP-MS. The measurements were performed in single spot mode with

144 a repetition rate of 10 Hz, fixed spot size diameter of 40 μm and a laser fluence of ~3.0 J/cm^2 on the

145 sample surface. The He flow rate in the sample chamber and in the HelEx II cup was set to 0.510 and

146 0.240 L/min, respectively. The MC-ICP-MS is a Neptune *XT* (Thermo Fischer Scientific), equipped

147 with 9 Faraday cups and 1 ion counter in the central position. The instrument is equipped with 0.8 X-

148 skimmer (Ni) + 0.8 Jet sample (Ni) cones and a large dry interface pump (Jet Pump), ensuring the

149 maximum sensitivity for isotopic determinations. Two Faraday collectors (L2 and H4) connected to

150 10^{11} Ω resistors were used for the simultaneous acquisition of the ^{10}B and ^{11}B intensities. The isobaric

151 interferences of $^{40}Ar^{4+}$ and $^{20}Ne^{2+}$ on $^{10}B^+$ were resolved working at low-resolution mode and the

152 interference on ^{11}B by $^{10}B^1H^+$ was negligible. Each analysis consisted of 30 cycles of background

153 followed by 40 cycles of data acquisition and 8 cycles of wash time, for a total of 78 cycles of ~ 1 s

154 each. Data reduction was carried out offline with an *in-house* spread sheet; $^{11}B/^{10}B$ ratios exceeding

155 2σ have been discharged. No downhole isotope ratio fractionation was observed.

156   Instrumental and laser-induced isotope fractionation was corrected using the standard-sample

157 bracketing protocol. The IAEA B4 tourmaline was analyzed as external standard ($\delta^{11}B$ = -8.62 ±

158 0.17‰ (2σ), Tonarini et al. 2003). The results are reported in the common delta(δ)-notation as permil

159 (‰) and expressed relative to the isotopic ratio of the NIST SRM951 boric acid ($^{11}B/^{10}B$ = 4.04362

160 ± 0.00137 (2σ); Catanzaro et al. 1970) (Table 1). The tourmaline SY309 (Marschall et al. 2006) was

161 used as quality control sample, yielding a $\delta^{11}B$ of +21.23 ± 0.28‰ (1σ), which is within the

162 uncertainty of the published value of Marschall et al. (2006).

163

164   - ***Single-crystal X-ray and neutron diffraction***

165   After a preliminary check of the crystals' quality using a KUMA-KM4 four-circle X-ray

166 diffractometer, intensity data were collected from a prismatic crystal (0.06 x 0.120 x 0.260 mm^3) of

167 probertite, at 293 K, with a Rigaku XtaLABSynergy-i X-ray diffractometer, equipped with a

168 PhotonJet-i Mo*Kα* microfocus source and a HyPix-6000HE HPC detector, at the ESD-MI. A series

169 of collection runs were optimised using the *ad hoc* routine of the *CrysAlisPro™* suite (Rigaku –

170 Oxford Diffraction 2019), in order to maximize the reciprocal space coverage and the quality of the

6

171   intensity data, with an ω-scan strategy, step size of 0.5° and an exposure time of 1 s per frame. A total

172   number of 43411 Bragg reflections was collected up to $2\theta_{max}$ of 75° (with -10 ≤ h ≤ +10, -20 ≤ k ≤

173   +21 and -22 ≤ l ≤ +22), out of which 5500 were unique (R_{int} = 0.0616, Laue class 2/m) and 3952 with

174    $I_o>2\sigma(I_o)$, giving a metrically monoclinic unit-cell with: a = 6.5790(1), b = 12.5431(2), c = 13.4062(2)

175   Å, β = 100.011(1)° and V = 1089.45(3) Å^3. Using the *ABSPACK* routine, implemented in the

176   *CrysAlisPro^{TM}* package (Rigaku – Oxford Diffraction 2019), the intensity data were corrected for

177   Lorentz-polarization effects and X-ray absorption (with a semi-empirical protocol). The reflection

178   conditions were consistent with the space group $P2_1/c$. Intensity data were also processed with the *E-*

179   *STATISTICS* program, implemented in the *WinGX* package (Farrugia 1999): the statistics of

180   distributions of the normalized structure factors suggest that the structure of probertite is

181   centrosymmetric at ~65% likelihood (the Sheldrick's $\left|E^2-1\right|$ criterion is 0.890). Additional details

182   pertaining to the X-ray data are given in the CIF (deposited as supplementary material).

183   Neutron diffraction data were collected (at low temperature) using a large single crystal of

184   probertite of 3.1 x 1.5 x 1.5 mm^3, on the four-circle diffractometer D9 at the Institut Laue-Langevin

185   (ILL), Grenoble, France. The crystal was glued at the top of an aluminium pin and placed on a close-

186   circuit displex device operated at 20(1) K (Archer and Lehmann 1986). The experiment was

187   conducted with a wavelength of 0.8359 Å, obtained from a Cu(220) monochromator, and a small

188   two-dimensional area detector. The data collection strategy consisted of a series of ω-scans (for low-

189   Q reflections) or ω-2θ scans (for high-Q reflections), with ω-range varying as a function of the

190   instrument resolution curve. A total number of 2171 unique reflections were collected (with 0 ≤ h ≤

191   +9, 0 ≤ k ≤ +17 and −18 ≤ l ≤ +18), (R_σ = 0.0536), all with $I_o>2\sigma(I_o)$, with d_{min} = 0.71 Å. Integration

192   of the reflections intensity, along with background and Lorentz factor correction, were done with the

193   *Racer* program (written by Clive Wilkinson and Garry McIntyre, ILL integration program suite,

194   https://forge.ill.fr/projects/sxtalsoft/repository/show/racer). Absorption correction was applied, on

195   the basis of shape of the crystal and its composition, using the ILL program *Datap* (the current version

196   of this program is available online on https://forge.ill.fr/). The lattice was found to be metrically

197   monoclinic, with a = 6.578(3), b = 12.508(3), c = 13.369(5) Å, β = 99.93(3)° and V = 1083.4(7) Å^3,

198   and the reflection conditions were found to be consistent with the space group $P2_1/c$, in agreement

199   with the previous X-ray experimental findings. Additional details pertaining to the neutron diffraction

200   data are given in the CIF (deposited as supplementary material).

201   Two crystal-structure refinements, based on the X-ray (collected at 293 K) and neutron

202   (collected at 20 K) intensity data, were conducted in the space group $P2_1/c$ using the SHELXL-97

203   software (Sheldrick 1997, 2008). Neutral X-ray scattering factors (from the *International Tables for*

7

204   *X-ray Crystallography - Vol. C)* of Na, Ca, B, O and H were used for the X-ray refinement, whereas

205   neutron scattering lengths of Na, Ca, B, O and H were taken from Sears (1986). In order to correct the

206   secondary isotropic extinction effect, the formalism of Larson (1967) was used.

207   The starting structural model was that of Menchetti et al. (1982), without any H site. After the

208   first cycles of refinement (with anisotropic displacement parameters), convergence was rapidly

209   achieved for both the data sets (*i.e.*, neutron and X-ray), with a series of residual peaks in the final

210   difference-Fourier map of the nuclear or electron density (negative for the neutron refinement,

211   positive for the X-ray refinement). The negative residual peaks observed in the difference-Fourier

212   map of the nuclear density were assigned to the H sites for the next cycles of refinement, as H has a

213   negative neutron scattering length. The H population was first modelled on the basis of the neutron

214   data, and then implemented in the X-ray refinement. Ten independent H sites were located, all with

215   realistic H-bonding schemes. With such a complete structure model, convergence was rapidly

216   achieved, the variance-covariance matrix showed no evidence of significant correlation among the

217   refined parameters, and the residuals in the difference-Fourier maps (of nuclear or electron density)

218   were not significant. All the principal mean-square atomic displacement parameters were positive

219   (including those for the H sites for the neutron refinement) and the final $R_1(F)$ was equal to 0.0566

220   (for 2171obs./ 281par.) for the neutron refinement and to 0.0402 (for 3952obs./ 230par.) for the X-

221   ray one. Some of the atomic displacement ellipsoids are significantly anisotropic at 20 K (CIF), likely

222   in response to a not efficient correction for the extinction effect with the isotropic model of Larson

223   (1967). Additional details pertaining to structure refinements are given in the CIF; selected

224   interatomic distances and angles are given in Table 2.

225

226   **Discussion and implications**

227   Chemical and crystallographic data of probertite here reported confirm the general formula

228   previously reported in the literature: $CaNa[B_5O_7(OH)_4]\cdot3H_2O$. Sr is the only potential substituent of Ca

229   (in its distorted polyhedron with CN = 9) experimentally observed, but its fraction is modest (*i.e.*, ~0.12

230   wt%, by LA-ICP-MS, Table 1); other potential substituents (*e.g.*, Ba) are insignificant. Consistently,

231   there is no evidence of significant substituents for Na (in its distorted polyhedron with CN = 6). Very

232   small fraction of Si (*e.g.*, ~0.05 wt%, by LA-ICP-MS, Table 1) were detected, likely to be ascribed to

233   micro-inclusions of quartz rather than a potential substituent of B in tetrahedral coordination. Other

234   potential substituents of B in tetrahedra are negligible (*e.g.*, Li or Be, Table 1). The concentration of

235   REE, or other industrially relevant elements, is not significant (Table 1). The $^{11}B/^{10}B$ ratio is 4.0385 ±

236   0.0008, which results in a $\delta^{11}B$ of -1.26 ± 0.20‰ (1σ). Such a depleted $\delta^{11}B$ value is consistent with

237 what usually expected from hydrothermal brines, in which the source of boron is more likely

238 ascribable to terrestrial reservoirs rather than to marine ones (e.g., Swihart and Moore 1986, Hussain

239 et al. 2021, and references therein). The virtually ideal chemical composition of probertite is in line

240 with the previous results recently reported for other borates: even colemanite ($Ca[B_3O_4(OH)_3]\cdot H_2O$,

241 Lotti et al. 2018, 2019), kurnakovite ($Mg[B_3O_3(OH)_5]\cdot 5H_2O$, Gatta et al. 2019) and kernite

242 ($Na_6[B_4O_5(OH)_4]_3\cdot 8H_2O$, Gatta et al. 2020) show no significant concentration of isomorphic

243 substituents, so that their experimental formulae are substantially identical to the ideal ones. On the

244 basis of the results that we have recently obtained on colemanite, kurnakovite, kernite and then

245 probertite, which come from different deposits, we can infer that the chemical purity of these minerals

246 cannot be ascribed to the conditions of a specific deposit, but it is rather a peculiarity of all the hydrous

247 borates occurring in lacustrine deposits with hydrothermal activity (with thermal spring origin for

248 boron). On one hand, the chemical purity is partially controlled by the crystal structure, and how

249 substituent elements can replace the nominal ones generating a low chemical strain: it is difficult to

250 find a potential substituent of B (in both CN 3 or 4), but Na and Ca could be efficiently replaced by

251 other alkaline or earth-alkaline cations. On the other hand, the chemical replacement can act only if

252 potential substituents are available in the growing environment, and thus it is governed even by the

253 composition of the solution. Gatta et al. (2020) offered a possible explanation, which can be extended

254 to all the hydrous borates occurring in lacustrine deposits with hydrothermal activity: iterated

255 dissolution and recrystallization could promote purification. As this process decreases the $\delta^{11}B$

256 imprint of the crystal due to Rayleigh fractionation effect (Oi et al. 1989), the B isotope composition

257 of the probertite documented here would require high pH fluids with relatively heavy $\delta^{11}B$ signature

258 in the initial stages (Palmer and Sturchio 1990; Palmer and Helvaci 1995). More studies, referred to

259 a statistically significant number of samples, are necessary to provide a robust model able to explain

260 the chemical purity of probertite and other borates occurring in this peculiar geological environment.

261 The X-ray and neutron structure refinements here reported confirm the general structural

262 model of probertite previously described by Menchetti et al. (1982). The structure is built on a

263 fundamental building unit represented by the so-called pentaborate polyanion $[B_5O_7(OH)_4]^{3-}$

264 (topology: $5(2\Delta + 3T)$), which consists of oxygen-sharing B-tetrahedra (with the B-ions in sp^3

265 electronic configuration) and -triangular units (with the B-ions in sp^2 electronic configuration) (Fig. 1).

266 The five (geometrical) components of the polyanion are: BO_3, BO_2OH, BO_4, BO_3OH and $BO_2(OH)_2$

267 groups. The pentaborate building units are connected to form infinite chains running along [100] (Fig.

268 1). Clusters, in the form of ribbons, of distorted Ca-polyhedra (CN = 9, see CIF and Table 2) and Na-

269 polyhedra (CN = 6, see CIF and Table 2) are mutually connected by edge-sharing and, in turn,

9

270   connected to the pentaborate chains by edge-sharing (with the Ca-polyhedron) and corner-sharing

271   (with the Na-polyhedron) (Fig. 1). More in details, the two independent structure refinements

272   consistently show that (numerical data pertaining to the neutron refinement):

1) The two triangular groups (*i.e.*, $B3O_3$ and $B5O_2OH$) have an almost ideal geometry, with $\Delta(B3\text{-}O)_{max} \sim 0.03$ and $\Delta(B5\text{-}O)_{max} \sim 0.04$ Å (*i.e.*, where Δ is the difference between the longest and the shortest B-O bond distances of this study), average O-B-O angles of 120° (ranging between 117.3°-122.0° for B3- and 115.2°-124.0° for B5-triangular groups), and aplanarity < 1° (here defined as the average angle described by the plane on which the 3-oxygen sites lie and each of the three independent B-O_n vectors) (CIF, Table 2). The tetrahedral BO_4, BO_3OH and $BO_2(OH)_2$ groups are only slightly distorted, with: $\Delta(B1\text{-}O)_{max} \sim 0.04$ Å, $<O\text{-}B1\text{-}O> \sim 109.5°$ and $\Delta(O\text{-}B1\text{-}O)_{max} \sim 9.0°$; $\Delta(B2\text{-}O)_{max} \sim 0.03$ Å, $<O\text{-}B2\text{-}O> \sim 110.1°$ and $\Delta(O\text{-}B2\text{-}O)_{max} \sim 6.6°$; $\Delta(B4\text{-}O)_{max} \sim 0.04$ Å, $<O\text{-}B4\text{-}O> \sim 109.5°$ and $\Delta(O\text{-}B2\text{-}O)_{max} \sim 7.9°$. It is worth to note that the longest distances are not ascribable to the B-OH bonds, as *e.g.,* B4-O9 is 1.500(3) Å whereas B4-O11H4 is 1.460(3) Å long. The long B4-O9 distance reflects the general bonding scheme of O9, as bridging site between B5 and B4 and bonded even to the Na site (with Na-O9 = 2.342(4) Å) (CIF, Table 2).

2) The Ca-polyhedron (CN = 9, $CaO_5(OH)_3(OH_2)$) and the Na-polyhedron (CN = 6, $NaO(OH)_2(OH_2)_3$) are strongly distorted, with Ca-$O_{min} \sim 2.39$ and Ca-$O_{max} \sim 2.84$ Å and Na-$O_{min} \sim 2.34$ and Na-$O_{max} \sim 2.64$ Å. The Ca-site is coordinated by five oxygen sites (O4, O5, O6 x 2 and O8), two hydroxyl groups (O1-H1, O10-H3 and O11-H4) and one H_2O molecule (H5-O12-H6). The Na-site is coordinated by one oxygen site (O9), two hydroxyl groups (O2-H2 and O11-H4) and three H_2O molecules (H5-O12-H6, H7-O13-H8 and H9-O14-H10) (Fig. 2, CIF, Table 2).

3) Three (crystallographically) independent H_2O molecules occur in the structure of probertite (*i.e.*, H5-O12-H6, H7-O13-H8 and H9-O14-H10, Table 2). Among those, two show an almost ideal geometrical configuration, with H5-O12-H6 = 104.9(4)° and H9-O14-H10 = 105.0(5)°, whereas the last one shows a "compressed" configuration with H7-O13-H8 = 100.4(4)°. All the O-H distances, corrected for "riding motion effect" (following the protocol of Busing and Levy 1964), range between 0.98 and 1.00 Å (Table 2). The H-bonding scheme of the three H_2O molecules is the following: for H5-O12-H6, the acceptors are the oxygen sites O7 and O13, with O12-H5...O7 = 161.0(4)° (O12...O7=2.856(3) Å) and O12-H6...O13 =157.4 (5)° (O12...O13=2.765(3) Å); for H7-O13-H8, the acceptors are the oxygen sites O14 and O2, with O13-H7...O14 = 163.3(4)° (O13...O14=2.747(3) Å) and

10

303   O13-H8...O2 =163.2(4)° (O13...O2=2.799(3) Å); for H9-O14-H10, the acceptors are the

304   oxygen sites O3 and O4, with O14-H9...O3 = 163.8(5)° (O14...O3=2.880(3) Å) and O14-

305   H10...O4 =173.9(4)° (O14...O4=2.715(3) Å) (Fig. 2, Table 2). Overall, the O_{donor}-

306   H…$O_{acceptor}$ angles are ≥ 157° and $O_{donor}…O_{acceptor}$ distances are ≤ 2.88 Å, approaching a

307   configuration energetically favourable (Table 2). The "compressed" configuration of the

308   H7-O13-H8 molecule is governed by the location of the two acceptor sites: O14 and O2 are

309   two vertices of the Na-polyhedron, confining one of its edges with O14↔O2 distance of

310   ~3.55 Å, thus forcing the molecule to a compressed geometry in order to keep the O14…H7-

311   O13-H8…O2 bonding scheme (Fig. 2). A similar scenario was also observed in other

312   minerals (*e.g.,* Gatta et al. 2008).

313   The four independent hydroxyl groups (*i.e.*, O1-H1, O2-H2, O10-H3 and O11-H4, CIF and

314   Table 2) show O-H distances, corrected for "riding motion effect" (Busing and Levy 1964),

315   ranging between 0.98-1.00 Å, $O_{donor}...O_{acceptor}$ distances between 2.7-3.3 Å, and O_{donor}-

316   H...$O_{acceptor}$ between 144-170°.

317   4)   The complex H-bonding net here described is consistent, at a first approximation, with the

318   IR spectrum of probertite reported in the RRUFF database (https://rruff.info/Probertite),

319   which contains at least six independent peaks, superimposed on a broad band (likely the

320   convolution effect of a series of additional peaks), in the range ascribable to the O-H

321   stretching region (*i.e.*, 3000-3700 cm^{-1}).

322   On the whole, the crystallochemical findings of this study prove that even in probertite,

323 consistently with what observed in other hydrous borates (Lotti et al. 2018, 2019; Gatta et al. 2019,

324 2020), the H-bonding network is complex and pervasive: 11 over 14 oxygen sites are involved in H-

325 bonds as *donor* or *acceptors* (Table 2). In this light, we can infer that the H-bonding network plays

326 in important role into the crystalline edifice, and a destabilization of the H-bonding scheme, for

327 example in response of the applied temperature or pressure or leaching, would lead to a phase

328 transition or even to a decomposition. The *P-T* stability of probertite, along with the mechanisms the

329 atomic scale under non-ambient conditions, are entirely unknown, and will be the aim of our future

330 experiments, based on *in situ* high-*P* and high-*T* X-ray diffraction investigations. In this respect, a

331 full knowledge of the H-bonding scheme, here described, is pivotal to understand the behaviour of

332 probertite under non-ambient conditions.

333   Beyond being a mineral commodity of B, probertite (with its ~50 wt% B_2O_3) could potentially

334 be a good candidate as a B-rich aggregate in concretes, used as radiation-shielding materials for the

335 pronounced ability of ^{10}B to absorb thermal neutrons. It is still unknown the solubility of probertite

11

336   in Portland or in Sorel cement pastes, along with its effects especially in the hardening stage. The

337   potential utilization of probertite in Portland cement concretes could be hindered by its high Na content

338   (~8.8 wt% Na_2O), which could potentially generate deleterious "alkali-silica reactions" – ASR,

339   undermining the durability of cements. On the other hand, the effect of B, Ca and Na in Sorel cements

340   (*i.e.*, magnesium oxychloride cements), commonly used to produce floor tiles and panels for fire

341   protection, is still unknown.

342

351

352

353

References

354   Archer, J. and Lehmann, M.S. (1986) A simple adjustable mount for a two-stage
356 cryorefrigerator on an Eulerian cradle. Journal of Applied Crystallography, 19, 456-459.

357   Barnes, W.H. (1949) The unit cell and space group of probertite. American Mineralogist, 34, 19-
358 25.

359   Busing, W.R. and Levy, H.A. (1964) The effect of thermal motion on the estimation of bond
360 lengths from diffraction measurements. Acta Crystallographica, 17, 142-146.

361   Carter, R.S., Palevsky, H., Myers, V.W., and Hughes, D.J. (1953) Thermal neutron absorption
362 cross sections of boron and gold. Physical Review, 96, 716-721.

363   Catanzaro, F., Champion, C., Garner, E., Marinenko, G., Sappenfield, K., and Shields, W.
364 (1970) Boric acid: isotopic and assay standard reference materials. National Bureau of Standards
365 Special Publication, 260, 1–70.

366   Clark, J.R. and Christ C.L. (1959) Studies of borate minerals (V): Reinvestigation of the X-
367 ray crystallography of ulexite and probertite. American Mineralogist, 44, 712–719.

368   Comboni, D., Pagliaro, F., Gatta, G.D., Lotti, P., Milani, S., Merlini, M., Battiston, T.,
369 Glazyrin, K., and Liermann, H.-P. (2020a) High-pressure behavior and phase stability of
370 $Na_2B_4O_6(OH)_2 \cdot 3H_2O$ (kernite). Journal of the American Ceramic Society, 103, 5291–5301.

371   Comboni, D., Pagliaro, F., Gatta, G.D., Lotti, P., Battiston, T., Garbarino, G., and Hanfland,
372 M. (2020b) High-pressure behaviour and phase stability of $Ca_2B_6O_6(OH)_{10} \cdot 2(H_2O)$ (meyerhofferite).
373 Physics and Chemistry of Minerals, 47, 50 (doi: 10.1007/s00269-020-01117-3).

374   Eakle, A.S. (1929) Probertite, a new borate. American Mineralogist, 14, 427-430.

375   European Commission (2017) Critical Raw Materials for the EU. Document 52017DC0490,
376 https://ec.europa.eu/growth/sectors/raw-materials/specific-interest/critical_en.

377   Farrugia, L.J. (1999) WinGX suite for small-molecule single-crystal crystallography. Journal
378 of Applied Crystallography, 32, 837-838.

379   Gatta, G.D., Rotiroti, N., McIntyre, G.J., Guastoni, A., and Nestola, F. (2008) New insights
380 into the crystal chemistry of epididymite and eudidymite from Malosa, Malawi: a single-crystal
381 neutron diffraction study. American Mineralogist, 93, 1158-1165.

382   Gatta, G.D., Guastoni, A., Lotti, P., Guastella, G., Fabelo, O., and Fernandez-Diaz, M.T. (2019)
383 A multi-methodological study of kurnakovite: A potential B-rich aggregate. American Mineralogist,
384 104, 1315-1322.

385 Gatta, G.D., Guastoni, A., Lotti, P., Guastella, G., Fabelo, O., and Fernandez-Diaz, M.T. (2020)
386 A multi-methodological study of kernite, a mineral commodity of boron. American Mineralogist, 105,
387 1424–1431.

388 Griffin, W.L., Powell, W.., Pearson, N.J., and O'reilly, S.Y. (2008) *GLITTER*: data reduction
389 software for laser ablation ICP-MS. Laser Ablation-ICP-MS in the Earth Sciences: Current practices and
390 outstanding issues, 308-311. Mineralogical Association of Canada.

391 Hussain, S.A., Han, F.Q., Ma, Z., Hussain, A., Mughal, M.S., Han, J., Alhassan, A., Widory, D.
392 (2021) Unraveling Sources and Climate Conditions Prevailing during the Deposition of Neoproterozoic
393 Evaporites Using Coupled Chemistry and Boron Isotope Compositions (δ^{11}B): The Example of the Salt
394 Range, Punjab, Pakistan. Minerals, 11, 161.

395 Larson, A.C. (1967) Inclusion of secondary extinction in least-squares calculations. Acta
396 Crystallographica, 23, 664-665.

397 Lotti, P., Gatta, G.D., Comboni, D., Guastella, G., Merlini, M., Guastoni, A., and Liermann, H.P.
398 (2017) High-pressure behavior and *P*-induced phase transition of $CaB_3O_4(OH)_3\cdot H_2O$ (colemanite).
399 Journal of American Ceramic Society, 100, 2209-2220.

400 Lotti, P., Gatta, G.D., Demitri, N., Guastella, G., Rizzato, S., Ortenzi, M.A., Magrini, F.,
401 Comboni, D., Guastoni, A., and Fernandez-Diaz, M.T. (2018) Crystal-chemistry and temperature
402 behavior of the natural hydrous borate colemanite, a mineral commodity of boron. Physics and
403 Chemistry of Minerals, 45, 405-422.

404 Lotti, P., Comboni, D., Gigli, L., Carlucci, L., Mossini, E., Macerata, E., Mariani, M., and Gatta,
405 G.D. (2019) Thermal stability and high-temperature behavior of the natural borate colemanite: An
406 aggregate in radiation-shielding concretes. Construction and Building Materials, 203, 679–686.

407 Marschall, H.R., Ludwig, T., Altherr, R., Kalt, A., and Tonarini, S. (2006) Syros metasomatic
408 tourmaline: Evidence for very high-δ^{11}B fluids in subduction zones. Journal of Petrology, 47, 1915–
409 1942.

410 Menchetti, S., Sabelli, C., and Trosti-Ferroni, R. (1982) Probertite, $CaNa[B_5O_7(OH)_4]\cdot 3H_2O$:
411 a refinement. Acta Crystallographica, B38, 3072-3075.

412 Morgan, V. and Erd, R.C. (1969) Minerals of the Kramer borate district, California. California
413 Division of Mines and Geology Mineral Information Service, 22, pp. 143-153 and 165-172.

414 Noble, L.F. (1926) Borate deposits in the Kramer district, Kern County, California. U.S.
415 Geological Survey Bulletin, 785, 45-61.

416 Oi, T., Nomura, M., Musashi, M., Ossaka, T., Okamoto, M., and Kakihana, H. (1989). Boron
417 isotopic compositions of some boron minerals. Geochimica et Cosmochimica Acta, 53, 3189-3195.

14

418   Okutan, M., Yalçın, Z., İçelli, O., Ay, F., Boncukçuoğlu, R., Artun, O., and Delipınar D.
419   (2014) Electrical behavior of probertite by dielectric spectroscopy. High Temperature Materials and
420   Processes, 33, 545 – 552.

421   Pagliaro, F., Lotti, P., Battiston, T., Comboni, D., Gatta, G.D., Cámara, F., Milani, S., Merlini,
422   M., Glazyrin, K., and Liermann, H-P. (2021) Thermal and compressional behavior of the natural borate
423   kurnakovite, $MgB_3O_3(OH)_5 \cdot 5H_2O$. Construction and Building Materials, 266, 121094.

424   Palmer, M.R. and Sturchio, N.C. (1990). The boron isotope systematics of the Yellowstone
425   National Park (Wyoming) hydrothermal system: A reconnaissance. Geochimica et Cosmochimica Acta,
426   54, 2811-2815.

427   Palmer, M.R. and Helvaci, C. (1995) The boron isotope geochemistry of the Kirka borate deposit,
428   western Turkey. Geochimica et Cosmochimica Acta, 59, 3599-3605.

429   Palmer, M.R. and Swihart, G.H. (1996) Boron Isotope Geochemistry: An Overview. In L.M.
430   Anovitz, E.S. Grew (Eds.), Boron: Mineralogy, Petrology, and Geochemistry, Review in Mineralogy
431   33, Mineralogical Society of America, Chantilly, pp. 709-744.

432   Puffer, J.H. (1975) The Kramer borate mineral assemblage. Mineralogical Record, 6, 84-91.

433   Rauch, H., and Waschkowski, W. (2002) Neutron Scattering Lengths. In A.J. Dianoux, G.
434   Lander (Eds.), Neutron Data Booklet, first ed., Institut Laue Langevin, Grenoble, pp. 1-18.

435   Rigaku-Oxford Diffraction (2019) *CrysAlisPro*: Single Crystal X-ray diffraction data collection
436   and processing software. Rigaku Corporation (www.rigaku.com/products/crystallography/crysalis).

437   Rumanova, I.M., Kurbanov, K.M., and Belov, N.V. (1966) Determination of the crystal
438   structure of probertite $CaNa[B_5O_7(OH)_4] \cdot 3H_2O$. Soviet Physics - Crystallography, 10, 513-522.

439   Schaller, W.T. (1930) Borate minerals from the Kramer district, Mohave Desert, California.
440   U.S. Geological Survey Professional Paper, 158, 137-170.

441   Sears, V.F. (1986) Neutron Scattering Lengths and Cross-Sections. In K. Sköld and D.L.
442   Price, Eds., Neutron Scattering, Methods of Experimental Physics, Vol. 23A, Academic Press, New
443   York, pp. 521-550.

444   Sheldrick, G.M. (1997) SHELXL-97. Programs for crystal structure determination and
445   refinement. University of Göttingen, Germany.

446   Sheldrick, G.M. (2008) A short history of SHELX. Acta Crystallographica, A64, 112-122.

447   U.S.G.S. (2019) Mineral commodity summaries 2019. U.S. Geological Survey, 200 p., Reston,
448   Virginia, U.S.A.

449   Swihart, G.H. and Moore, P.B. (1986) Boron isotopic composition of marine and nonmarine
450   evaporite borates. Geochimica and Cosmochimica Acta, 50, 1297–1301.

15

451   Tonarini, S., Pennisi, M., Adorni-braccesi, A., Dini, A., Ferrara, G., Gonfiantini, R., Wiedenbeck,

452   M., and Gröning, M. (2003) Intercomparison of Boron Isotope and Concentration Measurements. Part

453   I : Selection, Preparation and Homogeneity Tests of the Intercomparison Materials. Geostandards

454   Newsletter, 27, 21–39.

455   Zhou, B., Michaelis, V.K., Yao, Y., Sherriff, B.L., Kroeker, S., and Pan Y. (2014) Density

456   functional theory study of the magnetic shielding mechanism for ^{11}B in pentaborate minerals: ulexite

457   and probertite. CrystEngComm, 45, 10418-10427.

458

459

460

461

462

463

464

16

465 Table 1. Trace element concentrations (in wt ppm) and B isotope composition (in ‰) of probertite
466 based on the LA-ICP-MS and LA-MC-ICP-MS data, respectively.
467

Analyzed isotope	Analyte symbol	Average (n = 10)	1σ
7	Li	0.392	0.091
9	Be	0.310	0.170
29	Si	535	125
39	K	<2.03	
45	Sc	<0.100	
49	Ti	0.955	0.587
51	V	0.846	0.131
53	Cr	<0.570	
55	Mn	0.113	0.052
59	Co	0.108	0.006
60	Ni	0.269	0.030
65	Cu	1.17	0.220
66	Zn	<0.200	
75	As	<0.093	
85	Rb	<0.062	
88	Sr	1230	230
89	Y	4.60	1.18
90	Zr	0.042	0.062
93	Nb	0.003	0.002
111	Cd	<0.053	
121	Sb	0.070	0.012
133	Cs	0.012	0.005
137	Ba	5.05	3.51
139	La	5.66	4.07
140	Ce	11.7	6.4
141	Pr	1.46	0.63
146	Nd	6.32	2.07
149	Sm	1.54	0.27
151	Eu	0.359	0.067
157	Gd	1.29	0.22
159	Tb	0.164	0.036
163	Dy	0.910	0.176
165	Ho	0.162	0.048
167	Er	0.447	0.131
169	Tm	0.060	0.015
173	Yb	0.283	0.096
175	Lu	0.030	0.010
177	Hf	<0.007	
181	Ta	0.001	0.001
182	W	0.006	0.003
208	Pb	<0.009	
232	Th	0.006	0.002
238	U	0.002	0.001
	$\delta^{11}B$	-1.26	0.20

468

469

470

471

17

472 Table 2. Relevant bond distances (Å) and angles (°) based on the X-ray refinement at 293 K and
473 neutron structure refinement at 20 K.

474

X-ray (T = 293 K)					
Ca-O5	2.3994(7)	O4-B1-O2	113.7(1)	O12-H5	0.90(1)
Ca-O8	2.4310(8)	O4-B1-O3	111.2(1)	O12-H5*	0.92
Ca-O12	2.4413(9)	O2-B1-O3	105.4(1)	O12...O7	2.877(1)
Ca-O10	2.4478(8)	O4-B1-O1	106.4(1)	H5...O7	2.02(1)
Ca-O4	2.4608(8)	O2-B1-O1	111.5(1)	O12-H5...O7	157(1)
Ca-O6	2.5061(7)	O3-B1-O1	108.5(1)		
Ca-O1	2.5489(9)			O12-H6	0.90(1)
Ca-O6	2.6877(8)	O4-B2-O6	110.8(1)	O12-H6*	0.92
Ca-O11	2.8380(8)	O4-B2-O5	111.3(1)	O12...O13	2.769(1)
		O6-B2-O5	105.2(1)	H6...O13	1.91(1)
Na-O9	2.3437(9)	O4-B2-O7	109.2(1)	O12-H6...O13	158(1)
Na-O14	2.3618(11)	O6-B2-O7	111.3(1)		
Na-O11	2.4228(9)	O5-B2-O7	109.0(1)	O13-H7	0.91(2)
Na-O12	2.4288(10)			O13-H7*	0.93
Na-O2	2.4704(10)	O8-B3-O5	122.0(1)	O13...O14	2.768(1)
Na-O13	2.6521(12)	O8-B3-O3	117.1(1)	H7...O14	1.86(2)
		O5-B3-O3	120.9(1)	O13-H7...O14	170(1)
B1-O4	1.456(1)				
B1-O2	1.470(1)	O11-B4-O6	113.7(1)	O13-H8	0.90(2)
B1-O3	1.478(1)	O11-B4-O8	110.4(1)	O13-H8*	0.92
B1-O1	1.483(1)	O6-B4-O8	105.3(1)	O13...O2	2.815(1)
		O11-B4-O9	107.6(1)	H8...O2	1.95(2)
B2-O4	1.463(1)	O6-B4-O9	111.5(1)	O13-H8...O2	162(2)
B2-O6	1.471(1)	O8-B4-O9	108.3(1)		
B2-O5	1.479(1)			O14-H10	0.89(1)
B2-O7	1.484(1)	O9-B5-O7	123.9(1)	O14-H10*	0.92
		O9-B5-O10	120.9(1)	O14...O4	2.728(1)
B3-O8	1.354(1)	O7-B5-O10	115.2(1)	H10...O4	1.84(1)
B3-O5	1.366(1)			O14-H10...O4	173(1)
B3-O3	1.373(1)	O1-H1	0.90(1)		
		O1-H1*	0.92	O14-H9	0.89(1)
B4-O11	1.455(1)	O1...O7	2.978(1)	O14-H9*	0.91
B4-O6	1.459(1)	H1...O7	2.21(2)	O14...O3	2.912(1)
B4-O8	1.492(1)	O1-H1...O7	143(1)	H9...O3	2.06(2)
B4-O9	1.494(1)			O14-H9...O3	160(1)
		O2-H2	0.88(1)		
B5-O9	1.350(1)	O2-H2*	0.90		
B5-O7	1.360(1)	O2...O13	3.384(1)		
B5-O10	1.386(1)	H2...O13	2.54(1)		
		O2-H2...O13	164(1)		
		O10-H3	0.90(1)		
		O10-H3*	0.92		
		O10...O3	2.722(1)		
		H3...O3	1.85(1)		
		O10-H3...O3	162(1)		
		O11-H4	0.90(1)		
		O11-H4*	0.92		
		O11...O1	2.816(1)		
		H4...O1	1.93(1)		
		O11-H4...O1	167(1)		

* Bond distance corrected for "riding motion" effect. following Busing and Levy (1964)

18

| *Neutron* (T = 20 K)					
Ca-O5	2.394(3)	O4-B1-O2	114.1(2)	O12-H5	0.970(5)
Ca-O8	2.428(3)	O4-B1-O3	111.4(2)	O12-H5*	0.992
Ca-O10	2.440(3)	O2-B1-O3	105.0(2)	O12...O7	2.856(3)
Ca-O12	2.444(3)	O4-B1-O1	106.4(2)	H5...O7	1.922(5)
Ca-O4	2.454(3)	O2-B1-O1	111.2(2)	O12-H5...O7	160.9(4)
Ca-O6	2.494(3)	O3-B1-O1	108.6(2)		
Ca-O1	2.536(3)			O12-H6	0.967(5)
Ca-O6	2.701(3)	O4-B2-O6	110.93(2)	O12-H6*	0.988
Ca-O11	2.836(4)	O4-B2-O5	111.49(2)	O12...O13	2.765(3)
		O6-B2-O5	104.89(2)	H6...O13	1.847(5)
Na-O9	2.342(4)	O4-B2-O7	109.20(2)	O12-H6...O13	157.4(5)
Na-O14	2.356(4)	O6-B2-O7	111.11(2)		
Na-O11	2.420(4)	O5-B2-O7	109.16(2)	O13-H7	0.973(5)
Na-O12	2.422(4)			O13-H7*	0.989
Na-O2	2.479(4)	O8-B3-O5	122.0(3)	O13...O14	2.747(3)
Na-O13	2.635(5)	O8-B3-O3	117.3(2)	H7...O14	1.801(5)
		O5-B3-O3	120.7(2)	O13-H7...O14	163.3(4)
B1-O4	1.453(3)				
B1-O2	1.475(3)	O11-B4-O6	113.6(2)	O13-H8	0.980(5)
B1-O3	1.480(3)	O11-B4-O8	110.9(2)	O13-H8*	1.001
B1-O1	1.488(3)	O6-B4-O8	105.7(2)	O13...O2	2.799(3)
		O11-B4-O9	107.4(2)	H8...O2	1.847(5)
B2-O4	1.466(3)	O6-B4-O9	110.9(2)	O13-H8...O2	163.2(4)
B2-O6	1.471(3)	O8-B4-O9	108.2(2)		
B2-O5	1.479(3)			O14-H10	0.981(5)
B2-O7	1.481(3)	O9-B5-O7	124.0(2)	O14-H10*	0.996
		O9-B5-O10	120.8(2)	O14...O4	2.715(3)
B3-O8	1.354(3)	O7-B5-O10	115.1(2)	H10...O4	1.738(5)
B3-O5	1.368(3)			O14-H10...O4	173.9(4)
B3-O3	1.381(3)	O1-H1	0.962(5)		
		O1-H1*	0.986	O14-H9	0.964(6)
B4-O11	1.460(3)	O1...O7	2.948(3)	O14-H9*	0.984
B4-O6	1.462(3)	H1...O7	2.115(6)	O14...O3	2.880(3)
B4-O8	1.490(3)	O1-H1...O7	143.9(4)	H9...O3	1.942(6)
B4-O9	1.500(3)			O14-H9...O3	163.7(4)
		O2-H2	0.954(6)		
B5-O9	1.350(3)	O2-H2*	0.982		
B5-O7	1.364(3)	O2...O13	3.354(4)		
B5-O10	1.389(3)	H2...O13	2.425(6)		
		O2-H2...O13	164.5(5)		
		O10-H3	0.984(5)		
		O10-H3*	1.002		
		O10...O3	2.708(3)		
		H3...O3	1.767(5)		
		O10-H3...O3	158.8(4)		
		O11-H4	0.971(5)		
		O11-H4*	0.988		
		O11...O1	2.807(3)		
		H4...O1	1.847(5)		
		O11-H4...O1	169.9(4)		

* Bond distance corrected for "riding motion" effect. following Busing and Levy (1964)

19

564   Figure 1. The crystal structure of probertite viewed down [100] (H-free model), along with the infinite
565   chains made by the pentaborate polyanion $[B_5O_7(OH)_4]^{3-}$(topology: $5(2\Delta + 3T)$] running along [100]
566   and the cluster of distorted Ca-polyhedra (CN = 9) and Na-polyhedra (CN = 6), mutually connected
567   by edge-sharing. Structure model based on the neutron structure refinement of this study (intensity
568   data collected at 20 K). Displacement ellipsoid probability factor: 70%.

569
570
571
572
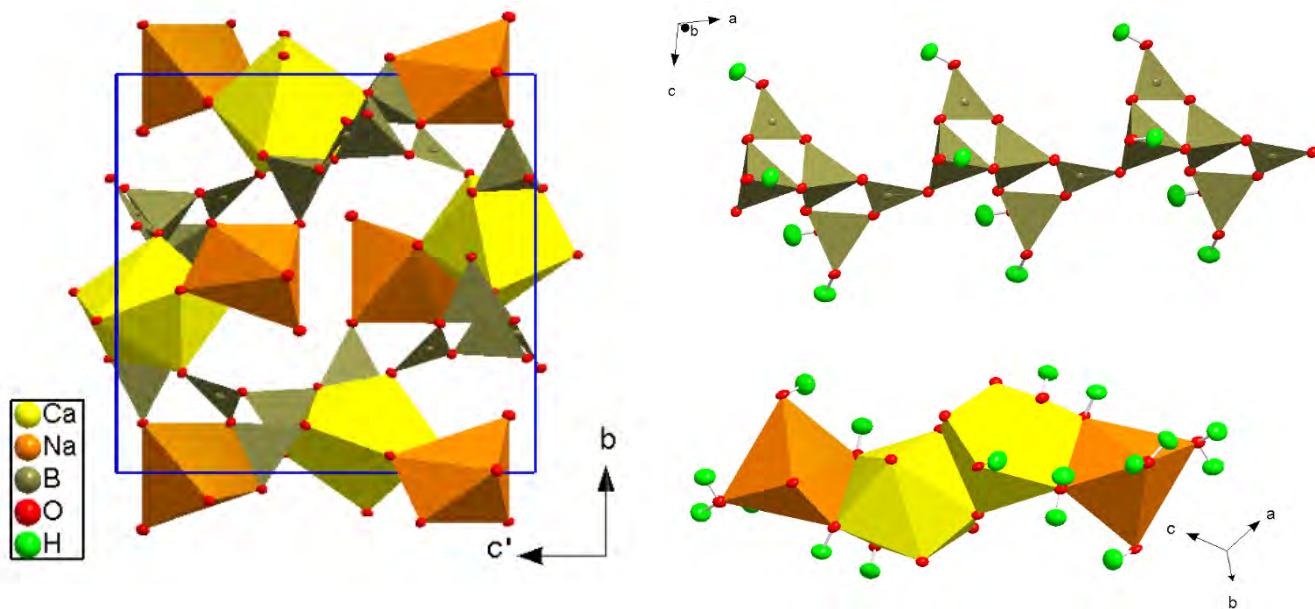
573
574
575
576
577
578
579
580

20

581 Figure 2. The complex H-bonding network into the crystal structure of probertite, based on the
582 neutron structure refinement (data collected at 20 K). Details in Table 2. Displacement ellipsoid
583 probability factor: 70%.
584
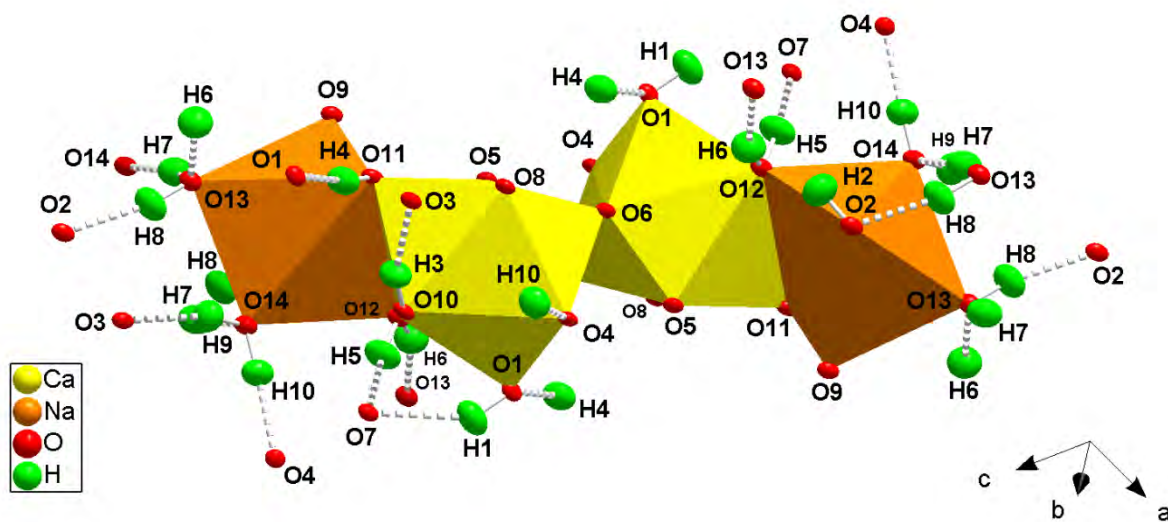
585
586
587
588
589
590
591
592
593
594
595
596
597
598
599
600
601
602
603
604
605
606
607
608
609
610
611
612
613
614
615

21